Published in final edited form as:

IEEE Trans Med Imaging. 2011 October ; 30(10): 1829–1840. doi:10.1109/TMI.2011.2154385.

PopTract: Population-Based Tractography

Pew-Thian Yap,
Department of Radiology and Biomedical Research Imaging Center (BRIC), University of North Carolina, Chapel Hill, NC 27599 USA

John H. Gilmore,
Department of Psychiatry, University of North Carolina, Chapel Hill, NC 27599 USA

Weili Lin, and
Department of Radiology and Biomedical Research Imaging Center (BRIC), University of North Carolina, Chapel Hill, NC 27599 USA

Dinggang Shen [Senior Member, IEEE]
Department of Radiology and Biomedical Research Imaging Center (BRIC), University of North Carolina, Chapel Hill, NC 27599 USA

Abstract

White matter fiber tractography plays a key role in the *in vivo* understanding of brain circuitry. For tract-based comparison of a population of images, a common approach is to first generate an atlas by averaging, after spatial normalization, all images in the population, and then perform tractography using the constructed atlas. The reconstructed fiber trajectories form a common geometry onto which diffusion properties of each individual subject can be projected based on the corresponding locations in the subject native space. However, in the case of high angular resolution diffusion imaging (HARDI), where modeling fiber crossings is an important goal, the above-mentioned averaging method for generating an atlas results in significant error in the estimation of local fiber orientations and causes a major loss of fiber crossings. These limitatitons have significant impact on the accuracy of the reconstructed fiber trajectories and jeopardize subsequent tract-based analysis. As a remedy, we present in this paper a more effective means of performing tractography at a population level. Our method entails determining a bipolar Watson distribution at each voxel location based on information given by all images in the population, giving us not only the local principal orientations of the fiber pathways, but also confidence levels of how reliable these orientations are across subjects. The distribution field is then fed as an input to a probabilistic tractography framework for reconstructing a set of fiber trajectories that are consistent across all images in the population. We observe that the proposed method, called PopTract, results in significantly better preservation of fiber crossings, and hence yields better trajectory reconstruction in the atlas space.

Correspondence to: Dinggang Shen.

Color versions of one or more of the figures in this paper are available online at http://ieeexplore.ieee.org.

Keywords

Brain circuitry; diffusion-weighted imaging; fiber tractography; population tractography; white matter

I. Introduction

Diffusion tensor imaging (DTI) [1] is a powerful imaging modality that allows probing into the intricate micro-architecture of white matter. It plays an indispensable role in characterizing neural pathways *in vivo* by means of fiber tractography, which entails reconstructing the trajectories of fiber paths by tracing the direction of maximal water diffusion. Such estimated fiber paths can subsequently be used, for instance, to investigate brain connectivity alterations in mental and neurological disorders [2], [3]. Tract pathology can be evident, as in the case of brain tumors where tracts are grossly displaced, or subtle, as in the case of neuropsychiatric disorders, such as schizophrenia where disruptions are manifested as change of diffusion properties within the tracts [4], [5].

The core assumption of DTI—Gaussianity of water diffusion—however, does not always hold true. This assumption implies that each imaging voxel can only be traversed by a single fiber bundle and, hence, it is sufficient to capture local fiber orientation by using a single direction vector. This can hardly be true considering the fact that current imaging technologies allow diffusion-weighted images to be acquired at a spatial resolution that is typically of the order of 2 mm, while the diameters of axon bundles considered in fiber tractography are of the order of 1 mm and individual physical neuronal fibers are of the order of 1–30 μm. Each imaging voxel hence captures water diffusion patterns that can be sophisticatedly heterogeneous. Modeling water diffusion using the single tensor formulation ignores this complexity and results in loss of information. It has in fact been shown that a significant fraction of the white matter (WM) voxels contain fiber bundle crossings [6], [7], in which case the simplistic model of DTI breaks down.

One of the methods proposed to remedy the shortcomings of DTI is high angular resolution diffusion imaging (HARDI) [8], where diffusion signals are acquired along a significantly larger number of directions than is normally employed in DTI. This allows modeling of the complex non-Gaussian diffusion process and construction of spherical functions with multiple local maxima which are potentially aligned with the underlying fiber bundle orientations. Accordingly, one naturally wants to extend existing DT-based tractography algorithms to work with HARDI data to better deal with fiber crossings and to reconstruct fiber trajectories that resemble more closely the anatomical fibers connecting different functional regions of the brain.

In this paper, we detail a tractography algorithm, called PoPTract, that allows effective reconstruction of fiber trajectories in the atlas space by more faithfully preserving fiber crossings. Tractography in the atlas space, as was done in previous works [9]-[11], allow the reconstructed trajectories to form a common geometry onto which diffusion properties from the individual images can be projected for tract-based comparison. To this end, a common step involves averaging the tensors [9]-[11], the fiber orientation distributions (FODs) [12],

or the diffusion signals [13] after spatial normalization, resulting in an atlas on which tractography can be performed after determining the local fiber orientations. We will show, however, that this approach causes significant deviation of the estimated local orientations from the "true" orientations. The major reason for this is the smearing of the orientation profile, caused by averaging misaligned ODFs (see Fig. 1). The cumulative effect of a fraction of a degree of error is detrimental for tractography algorithms, which are mostly greedy in nature, and can result in incorrect fiber trajectories that deviate significantly from the true fiber bundles.

Approaches alternative to the average atlas method includes clustering based approaches [14], [15] and reference tract based approach [16]. Clustering based approaches aim to group the fibers into bundles, which can then be compared between subjects. For instance, O'Donnell and Westin [14] utilize spectral clustering to automatically identify white matter structures that are related to expected anatomies, such as the corpus callosum, uncinate fasciculus, cingulum bundles, arcuate fasciculus, and corona radiata, thus making possible group comparison of fiber structures. Reference tract based approaches compare fibers or their representations based on a predefined reference tract. Clayden *et al.* [16], for example, transform the median lines of a set of fiber bundles into the space of a reference tract for comparison purposes.

In what follows, we will limit our discussion on average atlas based methods. We will show how PopTract can help im prove tractography accuracy, compared with an ODF-based average atlas approach. The average atlas is constructed by averaging the ODF fields of a population of subjects after spatial normalization.

A. Our Contribution

In our approach, local fiber orientation distributions are estimated by harnessing orientation information agglomorated from a population of diffusion-weighted images. Upon determining the fiber orientations from the local maxima of the ODFs [17], [18], PopTract models the orientation distribution at each voxel location by employing the bipolar Watson distribution [19], which captures the local mean fiber orientation and also the extent of orientation dispersion. We show that this orientation distribution information, when fed into a probabilistic tractography algorithm, allows better reconstruction of population-consistent fiber trajectories, compared with the average atlas approach.

In summary, the main thrust of this work is to design an effective population-based tractography algorithm in replacement of the conventional average atlas method to better exploit the power of HARDI in delineating complex orientational micro-structures. We discuss our approach in Section II, provide experimental results in Section III, and conclude the paper in Section IV.

II. Approach

The main idea of our approach is to model the orientation distribution at each voxel location by simultaneously considering all images in the population. Similar to the average atlas approach, we want to use this orientation information to reconstruct a set of fiber trajectories

that will form a common datum, based on which inter-subject tract-based morphometry can be performed. Unlike the average atlas approach, however, orientations are not estimated after, but prior to, averaging in the common space to avoid estimation inaccuracy caused by ODF smearing. The estimated orientation fields are transformed to a common atlas space where the maximum likelihood parameter estimates of the Watson distribution at each voxel location are determined. A probabilistic tractography algorithm is then used to reconstruct the fiber trajectories. A summary of the mathematical notations used in this paper is provided in Table I.

A. Modeling Local Fiber Orientations

1) Single Fiber Orientation—Assuming for a moment that the orientation fields computed from N diffusion-weighted images are spatially normalized to a common space and that each voxel location of an orientation field contains only one fiber orientation, our goal now is to accurately relate these orientations to an underlying model. At each voxel location of orientation field $i \in \{1,\ldots,N\}$, the local fiber orientation is denoted by a unit vector $\mathbf{v}_i$. We model the distribution of orientations across subjects using the bipolar Watson distribution [19], probability density function (PDF) of which is given by [20]

$$f(\mathbf{v}|\mu,\kappa) = C(\kappa)\, e^{\kappa(\mu^{\mathrm{T}}\mathbf{v})^2}. \quad (1)$$

The parameter $\boldsymbol{\mu}$ is a unit vector called the *mean orientation* and κ is a positive constant called the *concentration parameter*. The Watson distribution can be thought of as a bipolar symmetrization of the Fisher–Von Mises distribution [20], [21]. The squared exponential in (1) ensures that the distribution is antipodal symmetric. The density has maxima at $\pm\boldsymbol{\mu}$ and becomes more concentrated around $\pm\boldsymbol{\mu}$ as κ increases. The density is also rotationally invariant around $\pm\boldsymbol{\mu}$. $C(\kappa)$ is a normalizing constant to ensure that the density function integrates to unity over the unit sphere.

Assuming that the orientation vectors $\mathbf{v}_1,\ldots,\mathbf{v}_N$ are random samples from the Watson distribution, the maximum likelihood estimate (MLE) of $\boldsymbol{\mu}$ is the eigenvector corresponding to the largest eigenvalue λ_1 ($\lambda_1 \geq \lambda_2 \geq \lambda_3$) of the symmetric positive definite matrix [22]

$$\mathbf{A} = \frac{1}{N}\sum_{i=1}^{N} \mathbf{v}_i \mathbf{v}_i^{\mathrm{T}}. \quad (2)$$

Matrix $\mathbf{A}$ is called the *dyadic tensor* [23]. The MLE of κ is $(1-\lambda_1)^{-1}$, asymptotically when $\kappa \to \infty$ [22]. When $\kappa = 0$, the distribution is uniform. As κ increases, the PDF becomes more concentrated about $\pm\boldsymbol{\mu}$. Therefore, orientations that depart from $\pm\boldsymbol{\mu}$ are penalized more heavily when there is a strong alignment of the local fiber orientations from all subjects (see Fig. 2).

2) Extension to Multiple Fiber Orientations—Denoting the maximum number of possible orientations as Ω, we now denote the set of orientation vectors at each voxel location as $\left\{\mathbf{v}_i^{[D]}\right\}$, where $D = 1,\ldots,\Omega$. In the case where there is less than D orientations, the surplus orientation vectors are simply set to nil. For DTI, Ω is limited to 1. For HARDI,

however, the representation models used often allows more than one fiber orientations; hence $\Omega \geq 1$. During the course of a typical diffusion-weighted experiment, the average displacement of water molecules is expected to be of the order of 10 μm. Because it is not likely that water molecules will be able to visit regions of the sample separatedby more than a few tens of microns over the time scale of the diffusion time, we can assume that there is effectively no exchange between spatially distinct fiber bundles. We therefore estimate the parameters of the PDF for each compartment independently. That is, for the Dth compartment, we estimate $\boldsymbol{\mu}^{[D]}$ and $\boldsymbol{\kappa}^{[D]}$ using $\mathbf{v}_1^{[D]}, \ldots, \mathbf{v}_N^{[D]}$. For consistency, this is done after orientation sorting, as discussed next.

3) Orientation Sorting—When noise is present in diffusion-weighted images, ordering of the orientation vectors, especially in multi-orientation voxels, can be inconsistent. This results in a *sorting bias* [23], severity of which increases as the signal-to-noise ratio (SNR) decreases. To alleviate this problem, region-based sorting has been found to be effective [23]. Accordingly, we assume that the orientation field within a small neighborhood surrounding a point location is relatively homogenous and sort the orientations of the voxels in this neighborhood in tandem to ensure ordering consistency and reduce sorting bias. Specifically, for a particular spatial location, orientations in its neighborhood $\mathscr{M}$, are sorted to maximize cost function

$$\sum_{\substack{\mathbf{x}_1,\mathbf{x}_2\in\mathscr{M}\\ \mathbf{x}_1\neq\mathbf{x}_2}} \sum_{D} \rho^{[D]}(\mathbf{x}_1)\,\rho^{[D]}(\mathbf{x}_2) \left\{ \left[\mathbf{v}^{[D]}(\mathbf{x}_1)\right]^{\mathrm{T}} \mathbf{v}^{[D]}(\mathbf{x}_2) \right\}^2 \quad (3)$$

where $\rho^{[D]}(\mathbf{x})$ is the value of the ODF sampled at orientation $\mathbf{v}^{[D]}(\mathbf{x})$. For each voxel location $\mathbf{x} \in \mathscr{M}$, orientation vector $\mathbf{v}^{[D]}(\mathbf{x})$ is swapped with $\mathbf{v}^{[D+1]}(\mathbf{x})$ to gauge if the value of the cost function is reduced. If yes, the swap is maintained; otherwise, it is reverted. This is iterated until the global minimum of (3) is obtained. An illustration is given in Fig. 3.

4) Spatial Interpolation—In the process of transforming the orientation fields to the common space, interpolation is inevitable. For instance, the widely used trilinear interpolation involves computing, at a point location, a linear weighted average of eight neighboring voxels. However, interpolation, when done improperly, often results in information loss. To avoid this, we map all the eight neighboring voxels, linearly weighted by their distance to the point of interest, to the corresponding location in the common space and employ all of them for PDF parameter estimation.

B. Reconstructing Fiber Trajectories

A white matter fiber can be modeled as a finite-length path parameterized by a train of unit length vectors (see Fig. 4). We use the following notation for such a path: $\mathbf{v}_{(1:\tau)} = \left\{\mathbf{v}_{(1)}, \ldots, \mathbf{v}_{(\tau)}\right\}$. We further assume that the fiber path can be traced by tracking the trajectory of a particle travelling in an orientation field. Each particle is endowed with an initial speed in an appropriate direction. It then moves with constant speed to position $\mathbf{p}_{(t)}$ according to

$$\mathbf{p}_{(t+1)}=\mathbf{p}_{(t)}+s\mathbf{v}_{(t)} \quad (4)$$

where s is the step length. At each point in space, vector $\mathbf{v}_{(t)}$ is drawn from distribution

$$f\left(\mathbf{v}_{(t)}|\mathbf{v}_{(t-1)},\theta_{(t)},D_{(t)}\right) \quad (5)$$

where the set of parameters for the Watson distributions are collectively denoted as $\theta_{(t)}=\left\{\mu_{(t)}^{[1]},\ldots,\mu_{(t)}^{[\Omega]},\kappa_{(t)}^{[1]},\ldots,\kappa_{(t)}^{[\Omega]}\right\}$. Equation (5) is in fact the Watson distribution discussed in Section II-A. It is, however, now dependent on the prior orientation vector $\mathbf{v}_{(t-1)}$ in determining which orientation compartment $D(t) = 1,\ldots,\Omega$ to follow in the case where a voxel contains multiple orientations. Assuming that the Watson distribution is not directly dependent on $\mathbf{v}_{(t-1)}$ but only on $D(t)$, we can simplify $f(\mathbf{v}_{(t)}|\mathrm{v}_{(t-1)}, \theta_{(t)}, D_{(t)})$ to become $f(\mathbf{v}_{(t)}|\theta_{(t)}, D_{(t)})$. Specifically,

$$\begin{aligned} f & \left(\mathbf{v}_{(t)}|\mathbf{v}_{(t-1)},\theta_{(t)},D_{(t)}\right) \\ &= f\left(\mathbf{v}_{(t)}|\theta_{(t)},D_{(t)}\right) \\ &= C\left(\kappa_{(t)}^{\left[D_{(t)}\right]}\right)\mathrm{e}^{\kappa_{(t)}^{\left[D_{(t)}\right]}}\left(\left(\mu_{(t)}^{\left[D_{(t)}\right]}\right)^{\mathrm{T}}\mathbf{v}_{(t)}\right)^{2} \end{aligned} \quad (6)$$

and

$$\begin{aligned} f & \left(D_{(t)}|\mathbf{v}_{(t-1)},\theta_{(t)}\right) \\ &\propto \begin{cases} \bar{\rho}_{(t)}^{\left[D_{(t)}\right]}\left[\mathbf{v}_{(t-1)}^{\mathrm{T}}\mu_{(t)}^{\left[D_{(t)}\right]}\right]^{2}, & \left|\mathbf{v}_{(t-1)}^{\mathrm{T}}\mu_{(t)}^{\left[D_{(t)}\right]}\right| \geq cos\left(\phi\right) \\ 0, & \text{otherwise} \end{cases} \end{aligned} \quad (7)$$

where φ is the maximum allowed turning angle and $\bar{\rho}_{(t)}^{[D]}$ is defined as

$$\bar{\rho}_{(t)}^{[D]}=\frac{1}{N}\sum_{i=1}^{N}\rho_{i,(t)}^{[D]}. \quad (8)$$

with $\rho_{i,(t)}^{[D]}$ being the value of the ODF at the voxel location determined by $\mathbf{p}_{(t)}$, sampled at orientation $\mathbf{v}^{[D]}$. The tracing is stopped if the trajectory reaches a voxel with *orientation coherence* [24]

$$\beta^{[D]}=1-\sqrt{\frac{\lambda_2^{[D]}+\lambda_3^{[D]}}{2\lambda_1^{[D]}}},\quad \beta^{[D]}\in[0,1] \quad (9)$$

falling below a predefined threshold β_0, or simply when the brain boundary is encountered. The λ's are the eigenvalues of the dyadic tensor at each voxel location. Perfect alignment of the orientations in compartment D results in $\beta^{[D]} = 1$ and an uniform distribution of orientations results in $\beta^{[D]} = 0$.

An interpolation problem arises in the tracking process because orientation information is located on a discrete grid, whereas the tracked paths are not limited to such restriction. The probabilistic tractography framework allows us to employ the probabilistic interpolation method suggested by Behrens *et al.* [25], which utilizes the orientation information at a grid point chosen at random based on the distance to the current point location.

C. Summary—PopTract

After spatial normalization of the orientation fields to a common space [see Section III-B3], the steps involved in modeling the local fiber orientations and reconstructing the fiber trajectories are summarized as follows.

1) For each voxel location in the common space, estimate, for each orientation compartment D, the Watson distribution parameters $\boldsymbol{\mu}^{[D]}$ and $\kappa^{[D]}$.

2) Compute the coherence maps, $\beta^{[D]}$, $D = 1,\ldots,\Omega$, based on (9).

3) Decide on the seed voxel(s), maximum allowed turning angle φ, step length s, coherence threshold β_0, and number of trajectories Γ to initiate from each seed.

4) Initialize tracking at each seed and proceed in an orientation given by the Watson distribution.

5) At each location, compute the PDF (5), draw a random orientation, and proceed in the orientation.

6) Go to Step 5 unless $\beta < \beta_0$ or if the boundary of the brain is encountered.

7) Go to Step 4 and initialize another tract until the number of required trajectories Γ is fulfilled.

III. Results

We demonstrate in this section the effectiveness of the proposed method. We first present evaluation results using synthesized data, followed by results using *in vivo* adult and infant data.

A. Synthesized Dataset

To evaluate the effectiveness of the proposed method in preserving fiber crossings and in correctly estimating the orientations, we synthesized an 8 × 8 image (Camino [26]; two-tensor model) with each voxel containing a crossing with two orientations—one vertical and one horizontal. To simulate inter-subject variability, we perturbed the synthesized diffusion-weighted signal by applying random rotation matrices (angles: 15°, 30°, 45°, 60°) and adding isotropic complex Gaussian noise (SNR = 2, 4, 8, 16) to each voxel. The ODF at each voxel is then computed using Camino [26]. Samples of the ground truth and perturbed ODFs are shown in Fig. 5. We applied these perturbations 10 times to the no-noise image and then used the resultant images to attempt to recover the “true” population-based orientations. The orientations are determined by locating the local maxima of the ODF. We show, for qualitative evaluation, the results for the case of angle = 45° and SNR = 16 in Fig. 6. It can be observed that the average atlas method [Fig. 6(b)], generated by averaging the

ODFs, resulted in loss of fiber crossings and significant deviation in the estimated orientations. The proposed method [Fig. 6(c)] gave more consistent results.

For quantitative evaluation, we measured the orientational discrepency (OD) of the estimated orientations with respect to the ground truth orientations. Assuming that **U**(**x**) is the set of ground truth orientations at voxel location **x** and **V**(**x**) is the corresponding set of estimated orientations, OD is defined as

$$OD(\mathbf{x}) = \frac{1}{2}\left[\max_{\mathbf{u}\in\mathbf{U}(\mathbf{x})}\min_{\mathbf{v}\in\mathbf{V}(\mathbf{x})} d_\theta(\mathbf{u},\mathbf{v}) + \max_{\mathbf{v}\in\mathbf{V}(\mathbf{x})}\min_{\mathbf{u}\in\mathbf{U}(\mathbf{x})} d_\theta(\mathbf{v},\mathbf{u})\right] \quad (10)$$

where $d_\theta(\mathbf{u}, \mathbf{v})$ gives the angle difference between **u** and, i.e.,

$$d_\theta(\mathbf{u},\mathbf{v}) = cos^{-1}(|\mathbf{u}\cdot\mathbf{v}|). \quad (11)$$

The absolute value is taken since diffusion is assumed to be antipodal symmetric. In cases of multiple local maxima, the term

$$\min_{\mathbf{v}\in\mathbf{V}} d_\theta(\mathbf{u},\mathbf{v}) \quad (12)$$

returns the angle difference between **u** with an orientation **v** in **V** that is most closely aligned with itself. Evaluating the OD between the estimated orientations with the ground truth under different rotation angles and SNRs, the results, shown in Fig. 7, indicate that the proposed method is capable of estimating orientations which are closer to the ground truth, with improvement especially prominent when the angles of rotation is large. Fig. 8 is another rendition of Fig. 7, showing the relationship between the OD values with respect to different SNRs. The average atlas method seems not to benefit very much from the increase of SNR when the perturbation angle is large. In contrast, the proposed method shows a consistent decrease in orientation estimation error in all cases.

B. In Vivo Dataset

1) Materials—Diffusion-weighted images were acquired for 14 adult subjects using a Siemens 3T TIM Trio MR Scanner with an EPI sequence. Diffusion gradients were applied in 120 noncollinear directions with diffusion weighting b = 2000 s/mm^2, flip angle = 90°, repetition time (TR) = 12 400 ms and echo time (TE) = 116 ms. The imaging matrix was 128 × 128 with a rectangular FOV of 256 × 256 mm^2. Eighty contiguous slices with a slice thickness of 2 mm covered the whole brain. Data postprocessing includes brain skull removal, motion correction, and eddy current correction using algorithms developed and distributed as part of the FMRIB Software Library (FSL) package [27].

2) Orientation Estimation—The local maxima of an ODF reflect local fiber orientations. In our case, the orientations were computed with Camino [26] by locating the peaks of the ODFs using Powell's algorithm on a set of sample points generated by randomly rotating a unit icosahedron 1000 times. We limited the maximum number of orientations for each voxel to two. This choice is guided by several previous studies [28]-[30], where the estimation of two orientations is generally deemed as stable.

3) Spatial Normalization and Orientation Transformation—For spatial normalization, we employed an algorithm called *SPherical Harmonic Elastic REgistration* (SPHERE) [31]. SPHERE hierarchically extracts orientation information from HARDI data for structural alignment. The image volumes were first registered using robust, relatively direction invariant features derived from the ODF, and the alignment was then further refined using spherical harmonic (SH) representation with gradually increasing orders. This progression from nondirectional, single-directional to multi-directional representation provided a systematic means of extracting directional information given by diffusion-weighted imaging. Coupled with a template-subject-consistent soft-correspondence-matching scheme, this approach gave robust and accurate alignment of HARDI data. One image was selected, out of the 14 images, as the template onto which 13 other images were registered. The estimated transformations were used to map the respective orientation fields to a common space. When transforming the orientations, they were reoriented using $\mathbf{v}' = \mathbf{Fv}/\|\mathbf{Fv}\|$, where $\mathbf{F}$ is a local affine transform matrix computed from the image transformation map. For generating the average atlas, transformation of the ODF was performed based on a method similar to that proposed by Rafflet *et al.* [32], where we approximated the ODF using a number of weighted point spread functions (PSFs), reoriented these PSFs individually, and then recomposed the reoriented PSFs to obtain the transformed ODF. The same exact set of deformation fields, as applied to the orientation fields, were used to align the ODF fields. The average ODF at each voxel was then used to estimate the local fiber orientations.

4) Fiber Crossings—Similar to the results shown for the synthesized data (Fig. 6), significant loss of fiber crossings can be observed in the case of the *in vivo* data when the average atlas method is used for estimating the orientations (Fig. 9). For better understanding of the extent of the loss of crossings, we quantified the crossings in the regions given in Table II. These regions of interest (ROI) have been shown in [33], [34] to be traversed by crossing fibers. Guided by [35], these ROIs were drawn using ITK-SNAP [36] on the colored fractional anisotropy (FA) image of the template, and were then warped to the subject native spaces for quantification of crossings. For each voxel in these ROIs, we computed the ratio of the ODF value of the second orientation to the sum of ODF values of the first and second orientations as a measure of the relative strength of the second orientation. This gave us a better idea of how well the crossings were preserved. The results, as shown in Fig. 10, indicate that significantly better preservation of crossings can be observed in the left and right corona radiata and cingulum bundle regions compared with the average atlas method.

5) Tractography—For evaluation, we considered the following frequently studied fiber bundles.

- The forceps minor, also known as the anterior forceps, is a fiber bundle that connects the lateral and medial surfaces of the frontal lobes and crosses the midline via the genu of the corpus callosum.

- The forceps major, also known as the posterior forceps, is a fiber bundle that connects the occipital lobes and crosses the midline via the splenium of the corpus callosum.
- The cingulum is a medial associative bundle that runs within the cingulate gyrus all around the corpus callosum. It contains fibers of different lengths, the longest of which runs from the anterior temporal gyrus to the orbitofrontal cortex. The short U-shaped fibers connect the medial frontal, parietal, occipital, and temporal lobes and different portions of the cingulate cortex [37].
- The corticospinal tract is a collection of axons that travel between the cerebral cortex of the brain and the spinal cord.

To test whether these fiber bundles were preserved by the proposed method, we performed tractography based on seeds placed at the points where the midline crosses the genu and splenium of the corpus callosum, in the cingulate white matter, and in the cerebral peduncle. The tractography parameters used were $\varphi = 70°$, $\beta_0 = 0.1$, $s = 1$ mm, and $\varphi = 3000$. An identical set of parameters was used for the average atlas method. We note here that we are not targeting the forceps minor, forceps major, cingulum, and corticospinal tract *exclusively*; we reconstruct all fiber trajectories that are connected to the seeds and hence may result in extra fibers that do not belong to the intended fiber bundles. The results, shown in Fig. 11, indicate that the average atlas method results in premature termination of the fiber bundles. Specifically, in Fig. 11(a), we find that PoPTract, as opposed to the average atlas method, not only reconstructed the full forceps minor, with both frontal extensions of the fiber bundles intact, but also part of the anterior thalamic radiations. In Fig. 11(b), PoPTract shows a more complete reconstruction of the forceps major, posterior thalamic radiations, and tapetum. Similar conclusion can be made from Fig. 11(c), where PoPTract shows a complete reconstruction of the cingulum bundle and the U-shaped fibers connecting the medial frontal, parietal, occipital and temporal lobes. Fig. 11(d) shows that the corticospinal tract reconstructed by PoPTract extends deeper into the cerebral cortex, as indicated by the more yellowish color as the tract approaches the cortex, compared with the greenish color given by the average atlas method. It can therefore be concluded that PoPTract yields superior performance when compared with the average atlas method, producing a more accurate reconstruction of the fiber trajectories, which are more consistent with our anatomical knowledge of the bundles.

C. Infant Dataset

We show, as an application, how our method can be used to increase the reliability of the reconstructed fiber trajectories. For this purpose, we utilized a set of diffusion-weighted images acquired from a number of infants. We note that, images of newborns, unlike their one-/two-year-old or adult counterparts, are known to be of lower image quality in terms of SNR and resolution [38]-[40]. The fractional anisotropy [41] of their diffusion tensor images are also typically low, suggesting high uncertainty in orientation estimation. Our aim in this section is to demonstrate how the relatively higher level of noise affects tractography and how this is ameliorated using PoPTract.

1) Materials—Diffusion-weighted images of 10 infants were acquired at two time points: one month and one year after birth. Diffusion gradients were applied in 42 noncollinear directions with diffusion weighting $b = 1000$ s/mm^2, repetition time (TR) = 7680 ms and echo time (TE) = 82 ms. The scans covered the whole brain with a resolution of $2 \times 2 \times 2$ mm^3. Data postprocessing and orientation estimation steps similar to those described in Section III-B were performed for this dataset.

2) Longitudinal Spatial Normalization—To reduce alignment error caused by direct registration of the relatively low-quality newborn (one month time point) images, we employed a longitudinal registration strategy where the images of the newborns were first registered to their respective one year time point images. In this stage, only a small amount of deformation is required since intra-subject structural changes are generally much smaller compared with inter-subject variations. The estimated longitudinal deformations fields were then combined with the inter-subject deformations estimated using the one year time point images. Using the combined deformation fields, all the orientation fields of the newborn images were mapped to a common space, where tractography was then performed.

3) Tractography—Fig. 12(a) and (d) and Fig. 13(a) and (d) indicate that tractography using the template images alone falls short in terms of consistency since local fiber orientations in the newborn images might not be as reliable as in adult subjects. Fig. 12(a), for example, indicates that the forceps major tracked based on the template image alone at the one month time point is very noisy with spurious fibers that do not match well with our anatomical understanding of the fiber bundle [37], [42], [43]. In contrast, by using information gathered simultaneously from the 10 images, improved tractography results can be obtained [see Fig. 12(c)]. Note that with PopTract the reconstructed forceps major matches well across age, i.e., between the one month and one year time points, and with that of the adult subjects [see right panel of Fig. 11(b)]. With increased fiber maturation, a longer extension of the reconstructed fiber tracjectories in the anterior–posterior direction can be observed. It can also be observed that, with growth (i.e., fiber organization, membrane proliferation, and myelination [44]), more branching fibers can be detected by PopTract. This is clear in Fig. 12(f), where we can see that the fibers extend more lateral-wise into the cortical regions from the major bundle. The average atlas method, however, does not show a significant increase in branching fibers [compare Fig. 12(b) with (e)]. We also note that, due to maturation, fiber tracking in the one year time point template image becomes more reliable, as can be seen from Fig. 12(d), where the reconstructed forceps major seems quite reasonable. In this case, PopTract gives results which resemble more closely to that of the template image, compared with the average atlas method. Fig. 13 shows that considering simultaneous information from all images also gives a more complete reconstruction of the cingulum bundle with longer extensions to the anterior portion of the brain and also more U-shaped fibers connecting different brain cortical regions.

IV. Discussion

A. Diffusion Manifold

With better methods for estimating the average, such as by considering the proper manifold of the diffusion profiles, the performance of the average atlas method can perhaps be improved. For instance, averaging using log-Euclidean metrics [45] has been proved to be more effective in the case of DTI. Proper identification of the diffusion manifold is also a determining factor in the accurate interpolation of diffusion profiles since interpolation can be formulated as a convex combination problem in the manifold. The accuracy of the final constructed average atlas is also influenced by the choice of diffusion profile retransformation methods [32], [46], [47].

PopTract avoids direct averaging, interpolation and retrans-formation of the diffusion profiles. Instead, all these processes are combined in a unified framework via the estimated orientations. Of note, modeling orientation information using the Watson distribution inherently considers the manifold of the orientations. The geodesic distance between two orientations is captured via their squared scalar product, which decreases monotonically with the increase of the angle difference within the range of [0°,90°]. This allows PopTract to increase the SNR of the orientation information without indiscriminately averaging out useful information.

B. Deterministic Tractography

Probabilistic tractography can be computationally prohibitive, especially in studies involving whole brain connectivity [2], [3]. In these studies, whole brain seeding is often performed and probabilistic tractography will results in an intractably massive number of fibers. Our framework can be easily adapted to function deterministically so as to meet the need of such situations. This can be done by setting $\kappa \to \infty$ for all voxels and redefining (7) as

$$f\left(D_{(t)}|\mathbf{v}_{(t-1)},\theta_{(t)}\right) = \begin{cases} 1, & \text{if} \quad D_{(t)}=arg \quad max_{D'} \left\{ \bar{\rho}_{(t)}^{\left[D'\right]} \left[\mathbf{v}_{(t-1)}^{\mathrm{T}} \mu_{(t)}^{\left[D'\right]} \right]^2 \right\} \\ 0, & \text{otherwise.} \end{cases} \quad (13)$$

With this formulation, only one fiber trajectory is initiated for each seed and computation can be kept to a manageable level.

C. Groupwise Spatial Normalization

The registration methods employed in this current work is pairwise by nature. For unbiased atlas construction, groupwise registration methods can be employed [48]-[52]. Bias related to the template selection can be avoided by considering the population of images simultaneously when performing registration. Our future work would entail evaluating how PopTract can be improved with the use of groupwise registration. The current lack of which, however, does not affect the conclusion of this paper.

D. Advantages and Disadvantages

PopTract allows more accurate estimation of local fiber orientations for better reconstruction of fiber trajectories at a population level. But as with the average atlas based approaches in general, PopTract has a tendency of reconstructing trajectories that are common to all individuals but diminishes meaningful anatomical differences between individuals. If one is interested in characterizing the differences in connection topology between individuals, the clustering or reference tract based approaches mentioned in the introduction might be more suitable choices.

E. Concluding Remarks

We have presented a tractography algorithm, called PopTract, that is more effective in preserving fiber crossings and is more accurate in estimating local fiber orientations. PopTract results in more reasonable reconstruction of the fiber trajectories that are in closer agreement with known fiber bundles.

Acknowledgments

This work was supported in part by the National Institutes of Health under Grant EB006733, Grant EB008374, Grant EB009634, Grant MH088520, Grant HD05300, Grant MH064065, and Grant NS055754.

References

[1]. Alexander, DC. Visualization and Processing of Tensor Fields. Springer; Berlin, Germany: 2006. p. 83-106.

[2]. Yap P-T, Wu G, Shen D. Human brain connectomics: Networks, techniques, and applications. IEEE Signal Process. Mag. Jul; 2010 27(4):131–134.

[3]. Wee C-Y, Yap P-T, Li W, Denny K, Browndyke JN, Potter GG, Welsh-Bohmer KA, Wang L, Shen D. Enriched white matter connectivity networks for accurate identification of MCI patients. NeuroImage. 2010; 54(3):1812–1822. [PubMed: 20970508]

[4]. Ciccarelli O, Catani M, Johansen-Berg H, Clark C, Thompson A. Diffusion-based tractography in neurological disorders: Concepts, applications, and future developments. Lancet Neurol. 2008; 7(8):715–727. [PubMed: 18635020]

[5]. Kubicki M, McCarley R, Westin C-F, Park H-J, Maier S, Kikinis R, Jolesz FA, Shenton ME. A review of diffusion tensor imaging studies in schizophrenia. J. Psychiatric Res. 2007; 41:15–30.

[6]. Behrens T, Berg HJ, Rushworth JMFS, Woolricha M. Probabilistic diffusion tractography with multiple fibre orientations: What can we gain? NeuroImage. 2007; 34:144–155. [PubMed: 17070705]

[7]. Jeurissen, B.; Leemans, A.; Tournier, J-D.; Jones, DK.; Sijbers, J. ISMRM. Stockholm, Sweden: 2010. Estimating the number of fiber orientations in diffusion MRI voxels: A constrained spherical deconvolution study.

[8]. Tuch, DS.; Weisskoff, RM.; Belliveau, JW.; Wedeen, VJ. ISMRM. Philadelphia, PA: 1999. High angular resolution diffusion imaging of the human brain.

[9]. Yushkevich PA, Zhang H, Simon TJ, Gee JC. Structure-specific statistical mapping of white matter tracts. NeuroImage. 2008; 41:448–461. [PubMed: 18407524]

[10]. Goodlett CB, Fletcher PT, Gilmore JH, Gerig G. Group analysis of DTI fiber tract statistics with application to neurodevelopment. NeuroImage. 2009; 45(1):S133–S142. [PubMed: 19059345]

[11]. Zhang H, Awate SP, Das SR, Woo JH, Melhem ER, Gee JC, Yushkevich PA. A tract-specific framework for white matter morphometry combining macroscopic and microscopic tract features. Med. Image Anal. 2010; 14(5):666–673. [PubMed: 20547469]

[12]. Raffelt D, Tournier J, Fripp J, Crozier S, Connelly O, Salvado A. Symmetric diffeomorphic registration of fibre orientation distributions. NeuroImage. 2011

[13]. Bouix S, Rathi Y, Sabancu M. Building an average population atlas. MICCAI 2010 Workshop on Computational Diffusion MRI. 2010

[14]. O'Donnell LJ, Westin C-F. Automatic tractography segmentation using a high-dimensional white matter atlas. IEEE Trans. Med. Imag. Nov; 2007 26(11):1562–1575.

[15]. Wang Q, Yap P-T, Jia H, Wu G, Shen D. Hierarchical fiber clustering based on multi-scale neuroanatomical features. Med. Imag. Augment. Reality. 2010

[16]. Clayden JD, Storkey AJ, Bastin ME. A probabilistic model-based approach to consistent white matter tract segmentation. IEEE Trans. Med. Imag. Nov; 2007 26(11):1555–1561.

[17]. Descoteaux M, Angelino E, Fitzgibbons S, Deriche R. Regularized, fast, and robust analytical q-ball imaging. Magn. Reson. Med. 2007; 58:497–510. [PubMed: 17763358]

[18]. Hess CP, Mukherjee P, Han ET, Xu D, Vigneron DB. Q-ball reconstruction of multimodel fiber orientations using the spherical harmonic basis. Magn. Reson. Med. 2006; 56:104–117. [PubMed: 16755539]

[19]. Watson G. Equatorial distributions on a sphere. Biometrika. 1965; 52:193–201.

[20]. Jupp P, Mardia K. A unified view of the theory of directional statistics. Int. Stat. Rev. 1989; 57:261–294.

[21]. Banerjee A, Dhillon I, Gosh J, Sra S. Clustering on the unit hypersphere using von mises-fisher distributions. J. Mach. Learn. Res. 2009; 6:1345–1382.

[22]. Schwartzman A, Dougherty RF, Taylor JE. False discovery rate analysis of brain diffusion direction maps. Ann. Appl. Stat. 2008; 2(1):153–175.

[23]. Basser PJ, Pajevic S. Statistical artifacts in diffusion tensor MRI (DT-MRI) caused by background noise. Magn. Reson. Med. 2000; 44:41–50. [PubMed: 10893520]

[24]. Zhang H, Yushkevich PA, Alexander DC, Gee JC. Deformable registration of diffusion tensor MR images with explicit orientation optimization. Med. Image Anal. 2006; 10(5):764–785. [PubMed: 16899392]

[25]. Behrens T, Woolrich M, Jenkinson M, Johansen-Berg H, Nunes R, Clare S, Matthews P, Brady J, Smith S. Characterization and propagation of uncertainty in diffusion-weighted MR imaging. Magn. Reson. Med. 2003; 50(5):1077–1088. [PubMed: 14587019]

[26]. Cook PA, Bai Y, Nedjati-Gilani S, Seunarine KK, Hall MG, Parker GJ, Alexander DC. Camino: Open-source diffusion-MRI reconstruction and processing. Proc. 14th Sci. Meeting Int. Soc. Magn. Reson. Med. 2006:2759.

[27]. Smith S, Jenkinson M, Woolrich M, Beckmann C, Behrens T, Johansen-Berg H, Bannister P, Luca M, Drobnjak I, Flitney D, Niazy R, Saunders J, Vickers J, Zhang Y, Stefano N, Brady J, Matthews P. Advances in functional and structural MR image analysis and implementation as FSL. NeuroImage. 2004; 23:208–219.

[28]. Tuch D, Reese T, Wiegell M, Makris N, Belliveau J, Wedeen V. High angular resolution diffusion imaging reveals intravoxel white matter fiber heterogeneity. Magn. Reson. Med. 2002; 48:577–582. [PubMed: 12353272]

[29]. Peled S, Friman O, Jolesz F, Westin C-F. Geometrically constrained twotensor model for crossing tracts in DWI. Magn. Reson. Imag. 2006; 24(9):1263–1270.

[30]. Kreher B, Schneider J, Mader I, Martin E, Hennig J, Il'yasov K. Multitensor approach for analysis and tracking of complex fiber configurations. Magn. Reson. Med. 2005; 54(9):1216–1225. [PubMed: 16200554]

[31]. Yap P-T, Chen Y, An H, Yang Y, Gilmore JH, Lin W, Shen D. SPHERE: SPherical harmonic elastic REgistration of HARDI data. NeuroImage. 2011; 55(2):545–556. [PubMed: 21147231]

[32]. Raffelt, D.; Tournier, J-D.; Fripp, J.; Crozier, S.; Connelly, A.; Salvado, O. Non-linear spatial normalisation of high angular resolution diffusion imaging data using fiber orientation distributions; presented at the MICCAI Diffusion Modell. Fibre Cup; London, U.K.. 2009;

[33]. Alexander AL, Hasan KM, Lazar M, Tsuruda JS, Parker DL. Analysis of partial volume effects in diffusion-tensor MRI. Magn. Reson. Med. 2001; 45:770–780. [PubMed: 11323803]

[34]. Alexander D, Barker G, Arridge S. Detection and modeling of non-Gaussian apparent diffusion coefficient profiles in human brain data. Magn. Reson. Med. 2002; 48:331–340. [PubMed: 12210942]

[35]. Oishi K, Faria A, Jiang H, Li X, Akhter K, Zhang J, Hsu JT, Miller MI, van Zijl PC, Albert M, Lyketsos CG, Woods R, Toga AW, Pike GB, Rosa-Neto P, Evans A, Mazziotta J, Mori S. Atlas-based whole brain white matter analysis using large deformation diffeomorphic metric mapping: Application to normal elderly and alzheimer's disease participants. NeuroImage. 2009; 46:486–499. [PubMed: 19385016]

[36]. Yushkevich P, Piven J, Cody H, Ho S, Gee J, Gerig G. User-guided level set segmentation of anatomical structures with ITK-SNAP. Insight J. Nov.2005

[37]. Catania M, de Schottena MT. A diffusion tensor imaging tractography atlas for virtual in vivo dissections. Cortex. 2008:1–28. [PubMed: 19095231]

[38]. Shi F, Yap P-T, Fan Y, Gilmore JH, Lin W, Shen D. Construction of multi-region-multi-reference atlases for neonatal brain MRI segmentation. NeuroImage. 2010; 51(2):684–693. [PubMed: 20171290]

[39]. Shi F, Fan Y, Tang S, Gilmore JH, Lin W, Shen D. Neonatal brain image segmentation in longitudinal MRI studies. NeuroImage. 2010; 49(1):391–400. [PubMed: 19660558]

[40]. Shi F, Shen D, Yap P-T, Fan Y, Cheng J-Z, An H, Wald LL, Gerig G, Gilmore JH, Lin W. CENTS: Cortical enhanced neonatal tissue segmentation. Human Brain Mapp. 2010; 32:382–396.

[41]. Basser PJ, Pierpaoli C. Microstructural and physiological features of tissues elucidated by quantitative-diffusion-tensor MRI. J. Magn. Reson. 1996; (3):209–219. Series B 111.

[42]. Wakana S, Caprihan A, Panzenboeck MM, Fallon JH, Perry M, Gollub RL, Hua K, Zhang J, Jiang H, Dubey P, Blitz A, van Zijl P, Mori S. Reproducibility of quantitative tractography methods applied to cerebral white matter. NeuroImage. 2007; 36:630–644. [PubMed: 17481925]

[43]. Wakana S, Jiang H, Nagae-Poetscher LM, van Zijl PCM, Mori S. Fiber tract-based atlas of human white matter anatomy. Radiology. 2004; 230:77–87. [PubMed: 14645885]

[44]. Dubois J, Dehaene-Lambertz G, Perrin M, Mangin J-F, Coin-tepas Y, Duchesnay E, Bihan DL, Hertz-Pannier L. Asynchrony of the early maturation of white matter bundles in healthy infants: Quantitative landmarks revealed noninvasively by diffusion tensor imaging. Human Brain Mapp. 2007; 29:14–27.

[45]. Arsigny V, Fillard P, Pennec X, Ayache N. Log-Euclidean metrics for fast and simple calculus on diffusion tensors. Magn. Reson. Med. 2006; 56(2):411–421. [PubMed: 16788917]

[46]. Hong X, Arlinghaus L, Anderson A. Spatial normalization of the fiber orientation distribution based on high angular resolution diffusion imaging data. Magn. Reson. Med. 2009; 61(6):1520–1527. [PubMed: 19353649]

[47]. Geng X, Ross JT, Zhan W, Gu H, Chao Y-P, Lin C-P, Christensen GE, Schuff N, Yang Y. Diffusion MRI registration using orientation distribution functions. Proc. IPMI. 2009:627–637. LNCS 5636.

[48]. Jia H, Yap P-T, Wu G, Wang Q, Shen D. Intermediate templates guided groupwise registration of diffusion tensor images. NeuroImage. 2011; 54(2):928–939. [PubMed: 20851197]

[49]. Jia H, Wu G, Wang Q, Shen D. Absorb: Atlas building by self-organized registration and bundling. NeuroImage. 2010; 51(3):1057–1070. [PubMed: 20226255]

[50]. Wu G, Wang Q, Jia H, Shen D. Feature-based groupwise registration by hierarchical anatomical correspondence detection. Human Brain Mapp. 2011

[51]. Wang Q, Chen L, Yap P-T, Wu G, Shen D. Groupwise registration based on hierarchical image clustering and atlas synthesis. Human Brain Mapp. 2010; 31(8):1128–1140.

[52]. Wang Q, Wu G, Yap P-T, Shen D. Attribute vector guided groupwise registration. NeuroImage. 2010; 50(4):1485–1496. [PubMed: 20097291]

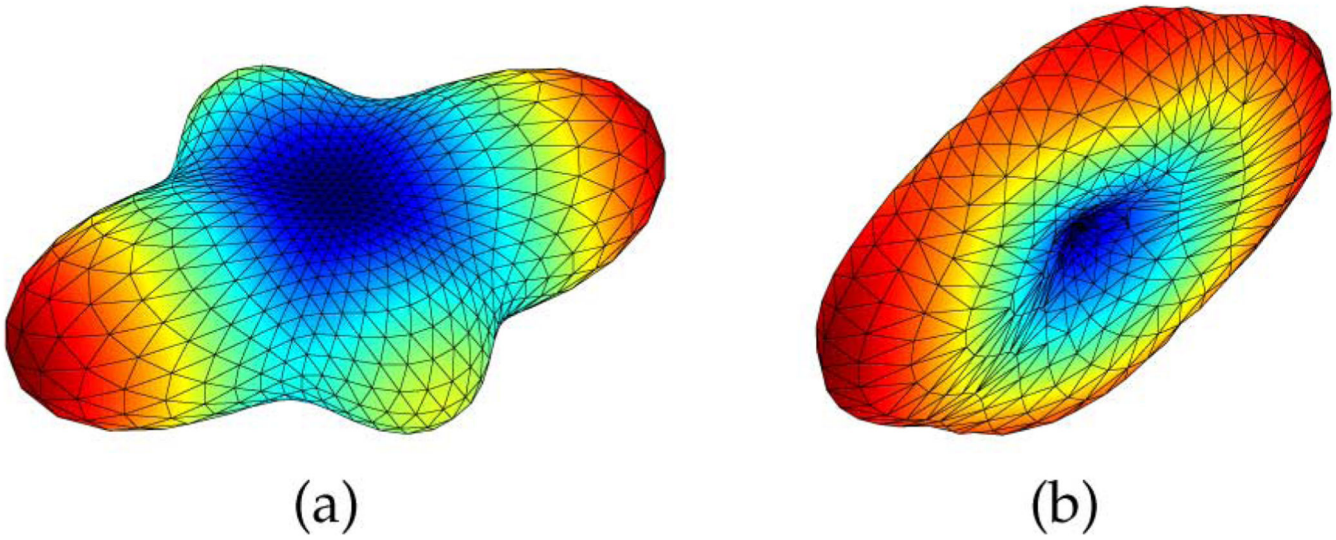

Fig. 1.
Smearing of the ODF. (a) The original ODF. (b) The ODF resulting from the averaging out-of-alignment ODFs simulated by perturbing the original ODF with slight random rotations.

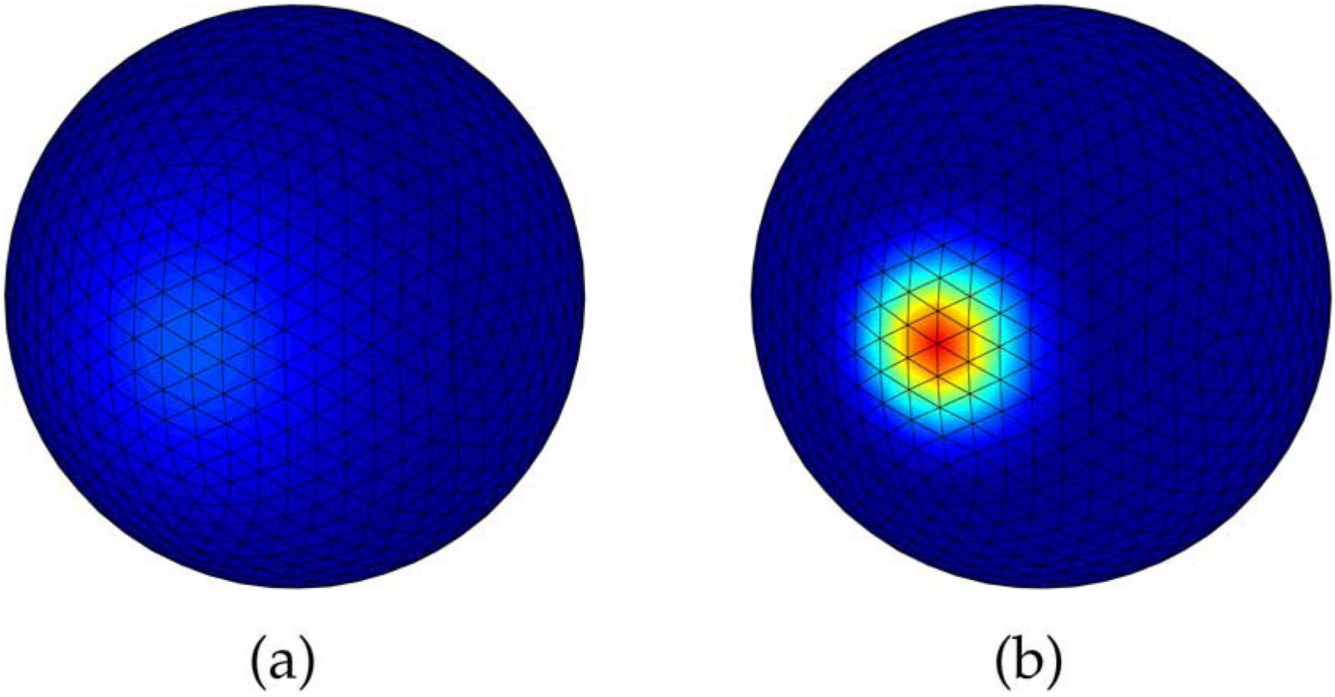

Fig. 2.

The Watson distribution is more concentrated around the mean orientation $\boldsymbol{\mu}$ when k has a larger value: (a) $\kappa = 4$, typical for a gray matter voxel, (b) $\kappa = 15$, typical for a voxel in the corpus callosum. Dark red indicates high probability values and dark blue indicates otherwise.

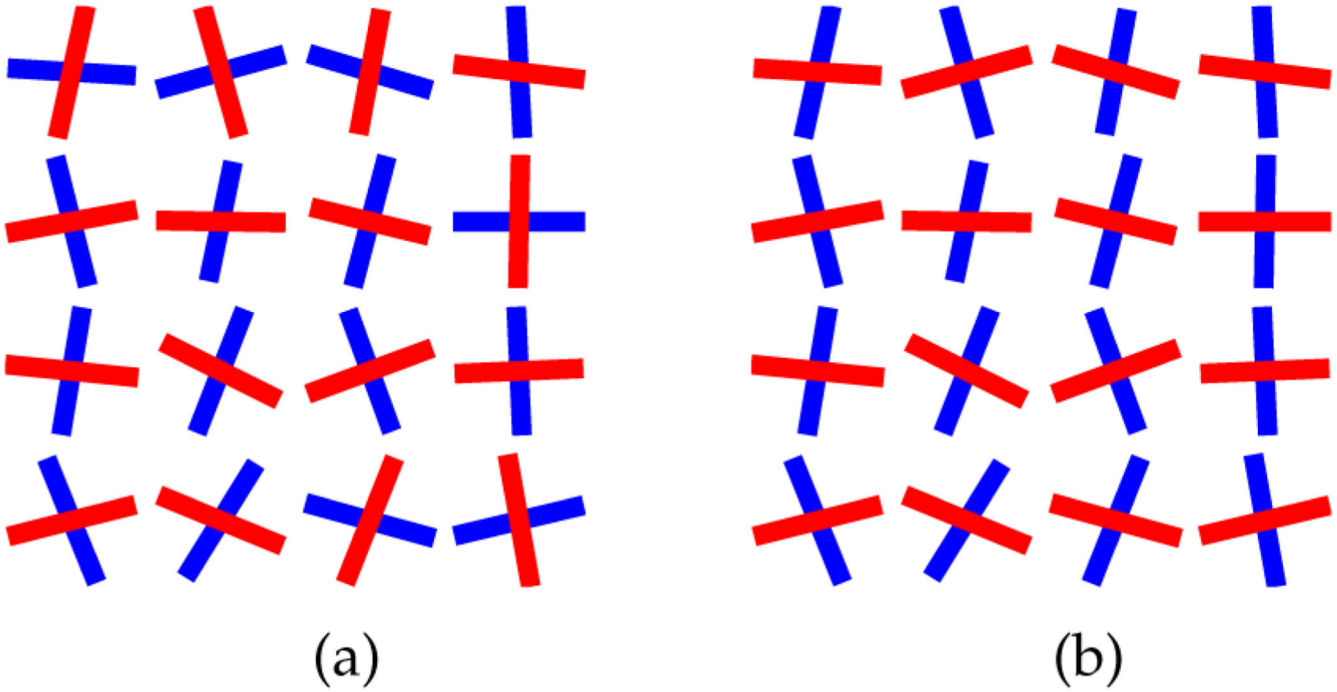

Fig. 3.

Orientation sorting. Note that, prior to sorting, the ordering of some of the red orientations and blue orientations is inconsistent. This is resolved by using the sorting algorithm described in Section II-A3. (a) Before sorting. (b) After sorting.

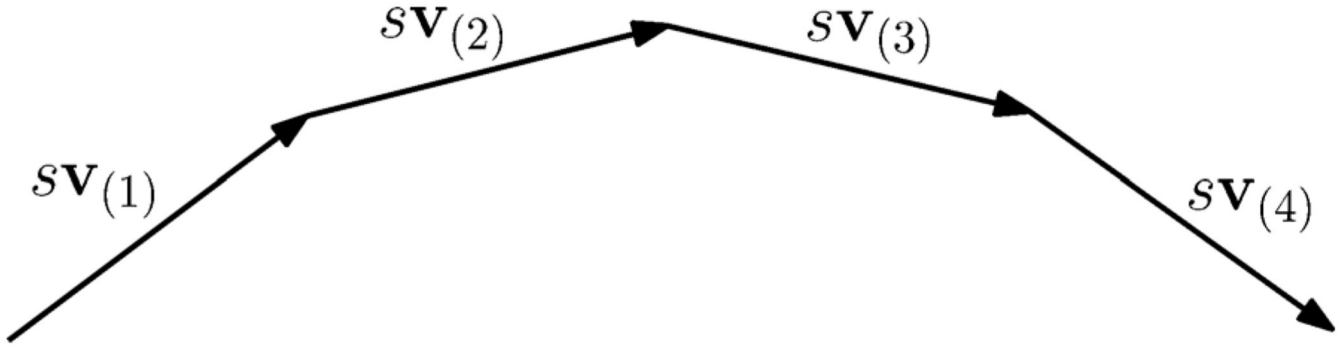

Fig. 4.
Fiber path is represented by a train of vectors, $\mathbf{v}_{(i)}$, with step length s.

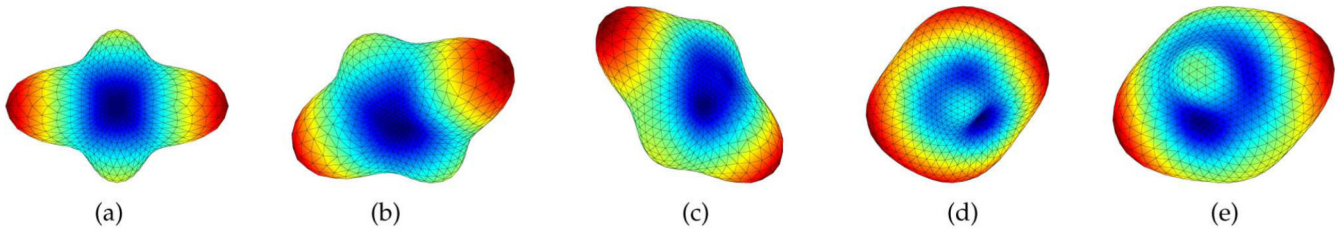

Fig. 5.

Synthesized ODFs perturbed with noise at different SNR levels. (a) Ground Truth, (b) SNR = 16, (c) SNR = 8, (d) SNR = 4, (e) SNR = 2.

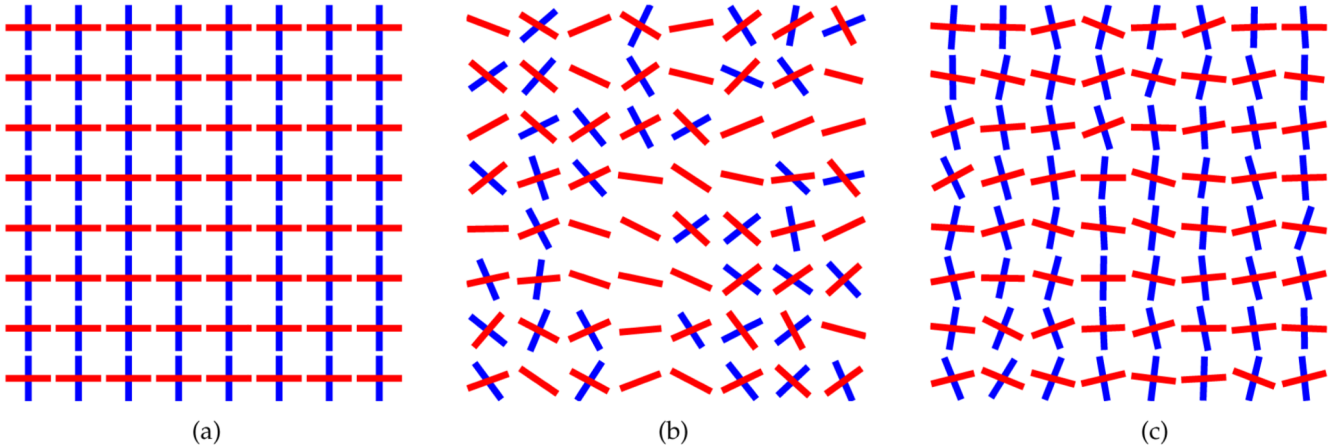

Fig. 6.

Estimation of population-based orientations using different schemes. (a) Ground truth. (b) Average atlas. (c) PopTract.

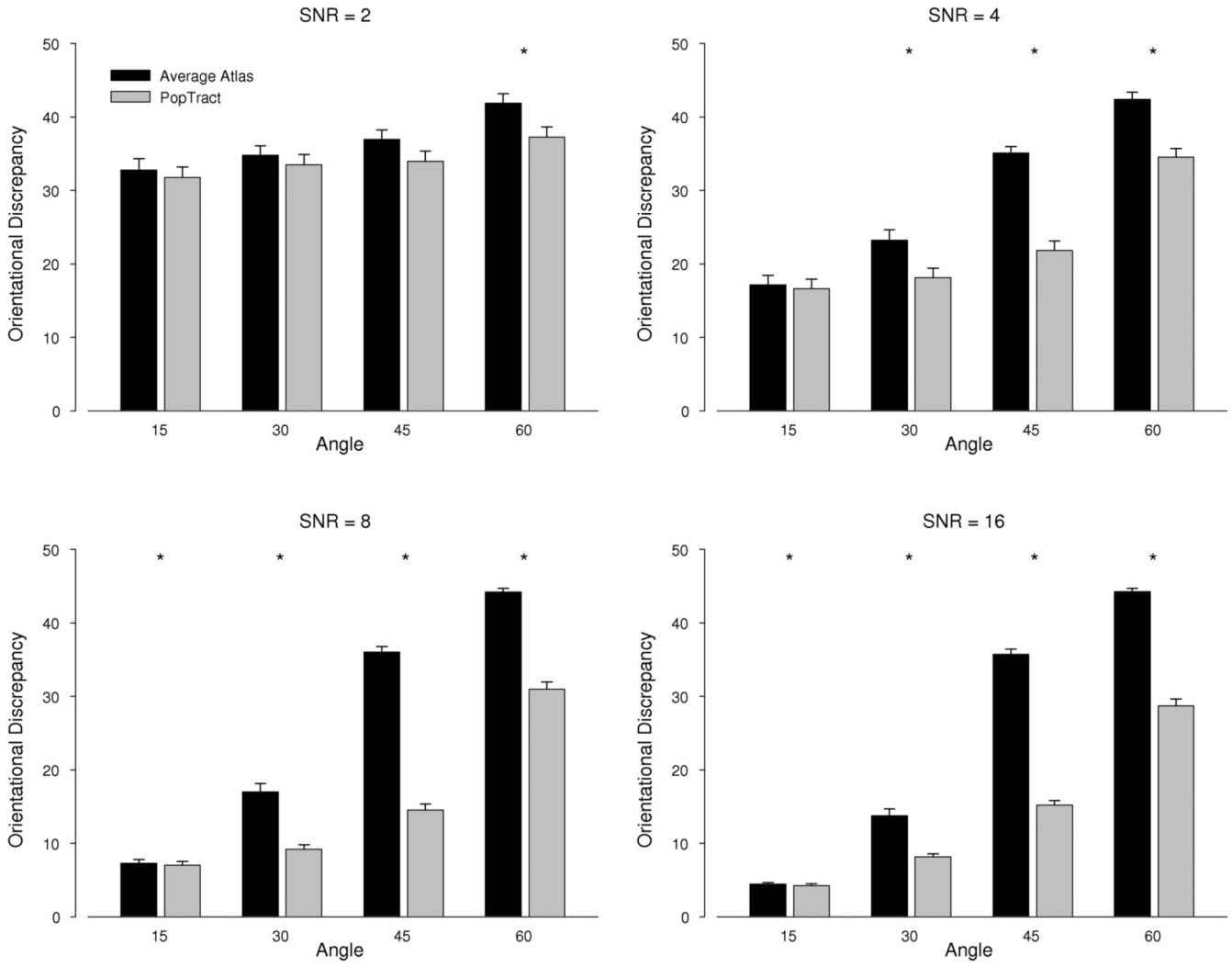

Fig. 7.

Orientational dicrepancy between the estimated orientations and the ground truth orientations under different rotation angles and signal-to-noise ratios. Each bar indicates the mean value, and the error bar indicates the corresponding standard error. The asterisks (*) mark differences that are statistically significant (paired *t*-test, $p = 0.05$).

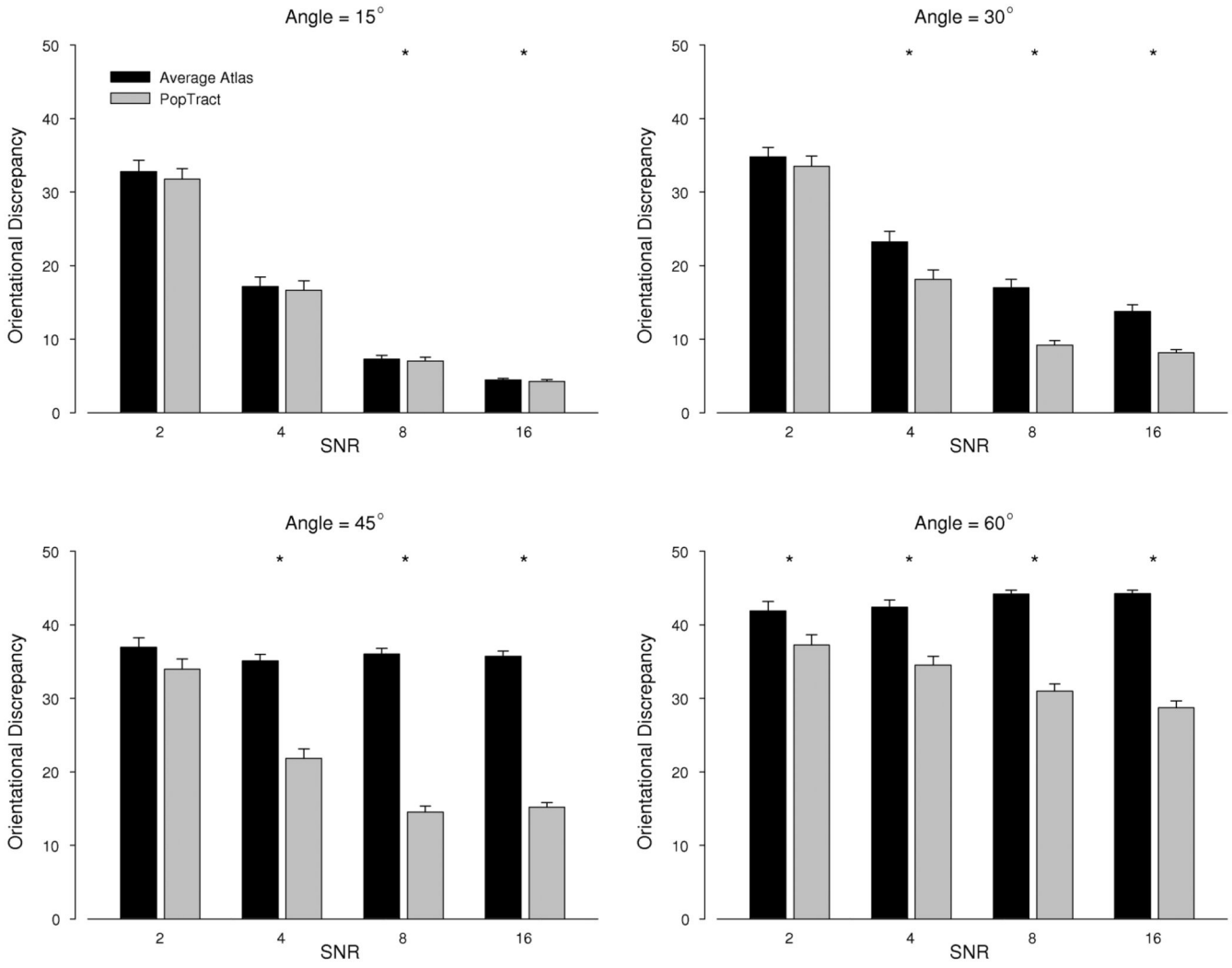

Fig. 8.

Orientational dicrepancy between the estimated orientations and the ground truth orientations under different rotation angles and signal-to-noise ratios. Each bar indicates the mean value, and the error bar indicates the corresponding standard error. The asterisks (*) mark differences that are statistically significant (paired *t*-test, $p < 0.05$).

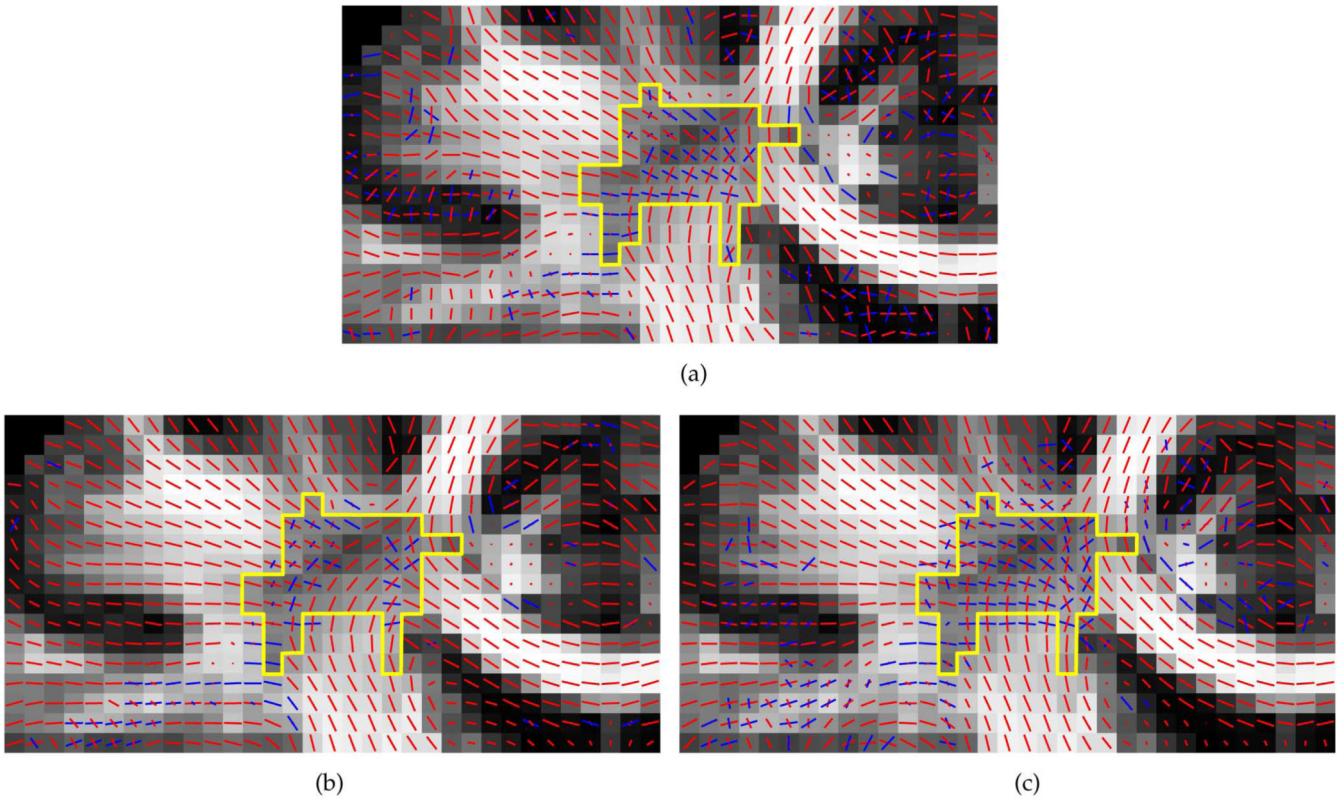

Fig. 9.

Fiber crossings. A significant loss of crossings can be observed for the average atlas method. (a) Template. (b) Average atlas. (c) PopTract.

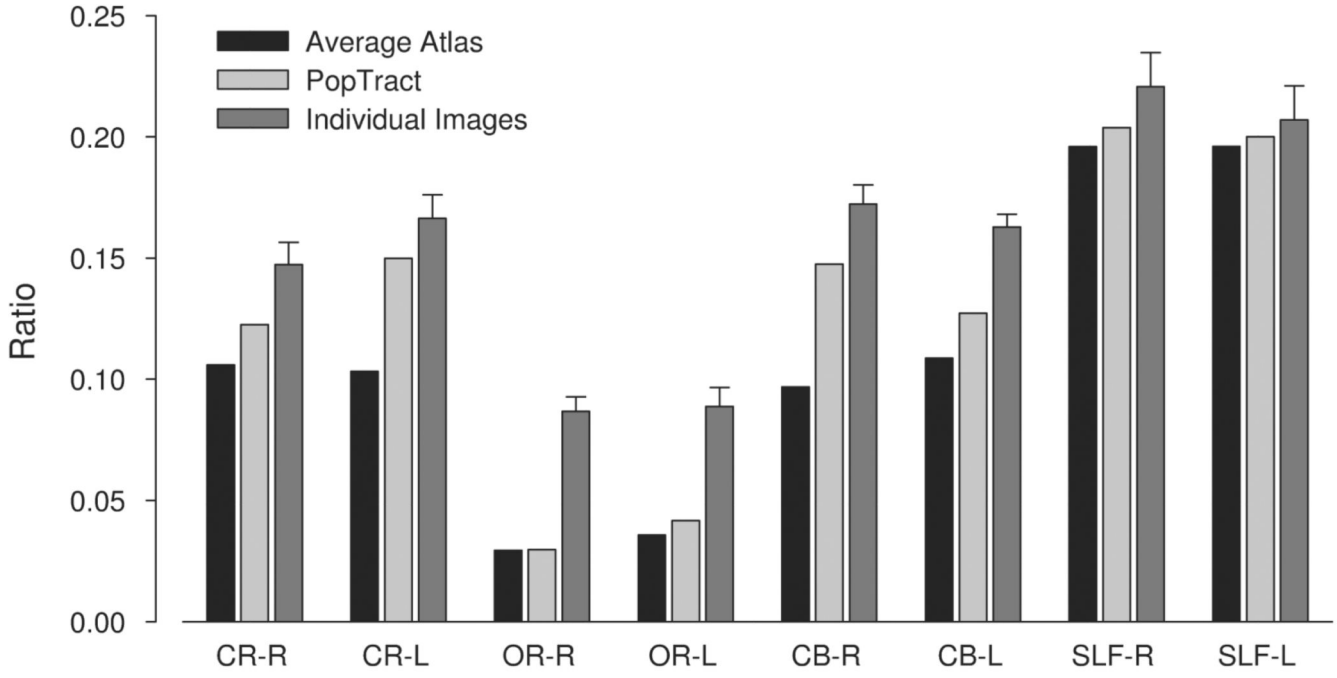

Fig. 10.

ODF ratios. Higher values indicate greater relative strength of the second orientation. Each bar indicates the mean value, and the error bar indicates the corresponding standard error. Error bars are shown only for “individual images,” since it is the only case where measurement variability can be computed based on a number of images.

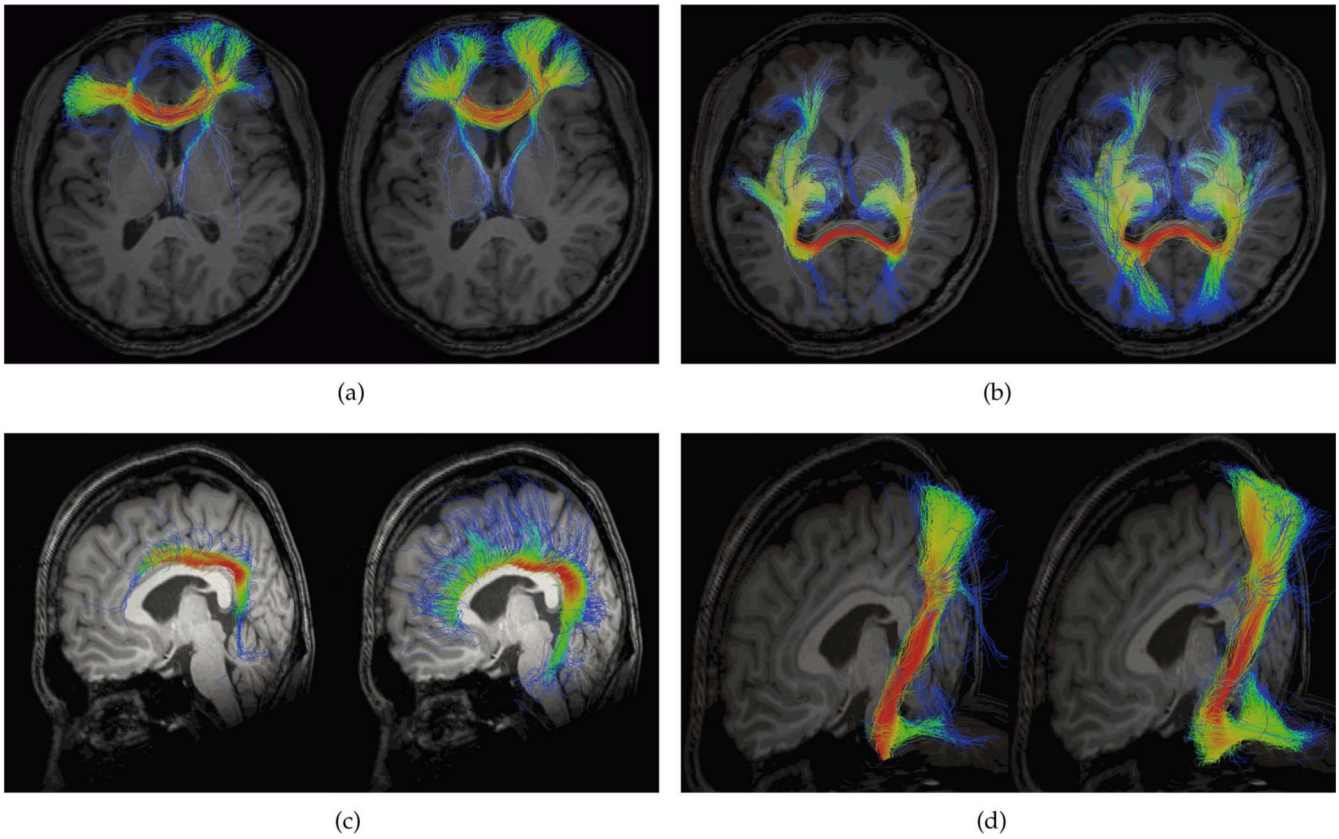

Fig. 11.

Fiber trajectory reconstruction of the (a) forceps minor, (b) forceps major, (c) cingulum bundle, and (d) corticospinal tract. The results given by the average atlas method and PopTract are shown on the left and right, respectively. The coloring indicates the probability of finding a fiber at a specific spatial location. Dark red indicates a high probability that a particular location is traversed by fibers; dark blue indicates otherwise.

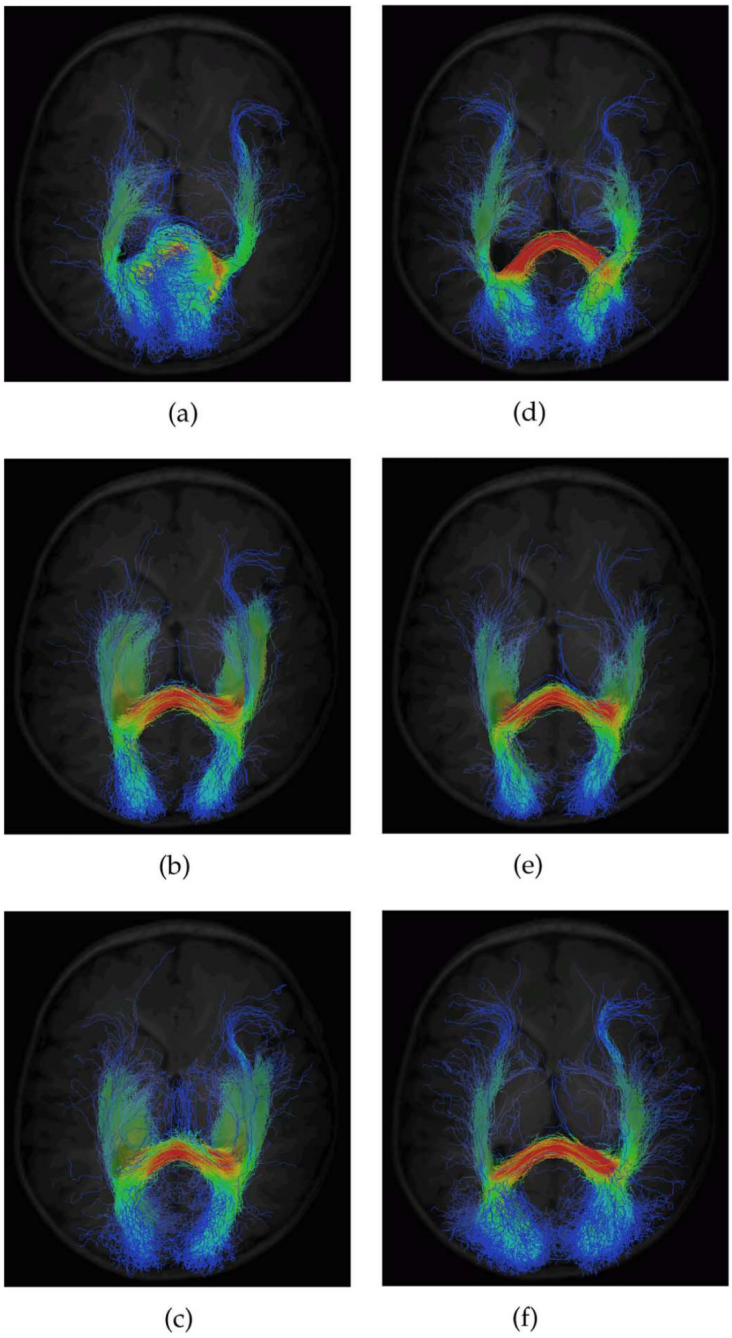

Fig. 12.

Fiber trajectory reconstruction of the forceps major of the infants at the one month (a)–(c) and one year (d)–(f) time points. The coloring indicates the probability of finding a fiber at a specific spatial location. Dark red indicates a high probability that a particular location is traversed by fibers, and dark blue indicates otherwise. (a) Template (one month). (b) Average atlas (one month). (c) $P_{OP}T_{RACT}$ (one month). (d) Template (one year). (e) Average atlas (one year). (f) $P_{OP}T_{RACT}$(one year).

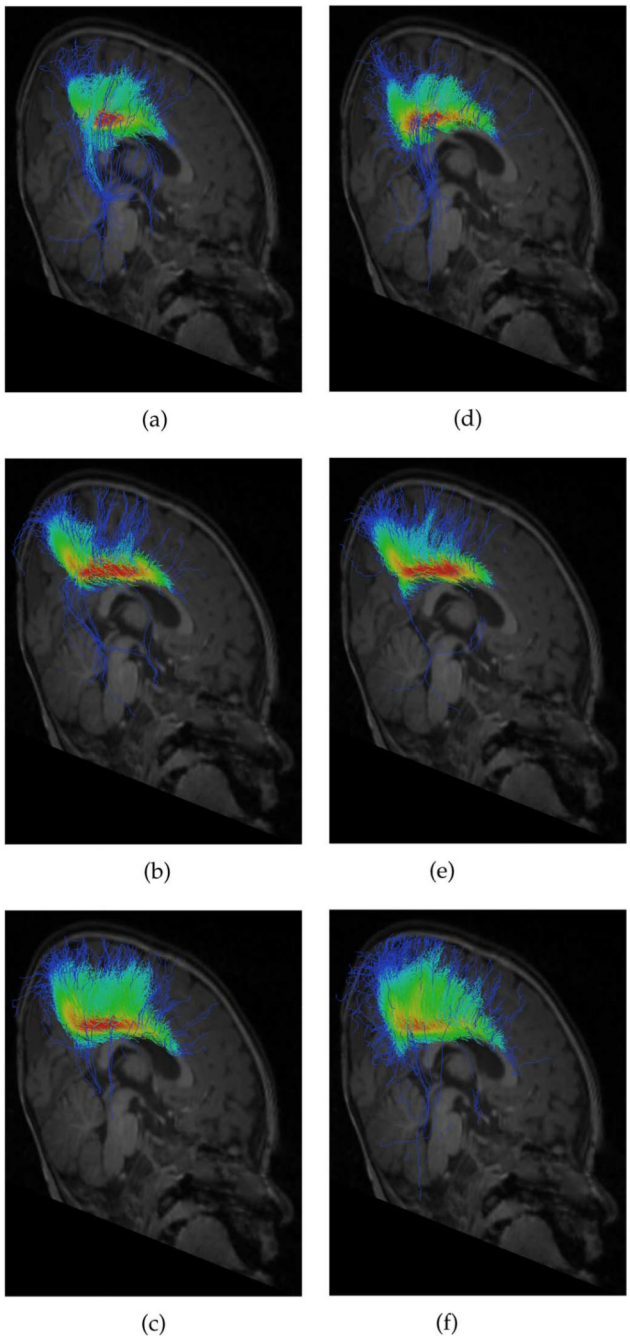

Fig. 13.

Fiber trajectory reconstruction of the cingulum bundle of the infants at the (a)–(c) one month and (d)–(f) one year time points. The coloring indicates the probability of finding a fiber at a specific spatial location. Dark red indicates a high probability that a particular location is traversed by fibers, and dark blue indicates otherwise. (a) Template (one month). (b) Average atlas (one month). (c) PopTract (one month). (d) Template (one year). (e) Average atlas (one year). (f) PopTract (one year).

TABLE I

Summary of Notations

Notation	Description
$\mathbf{u}, \mathbf{v}$	General orientation vectors
$\mathbf{v}_i$	An orientation vector at a particular voxel location of the orientation field of subject i
$\mathbf{v}_i^{[D]}$	A vector representing the D-th orientation at a particular voxel location of the orientation field of subject i
$\mathbf{p}_{(t)}$	The t-th point on a fiber trajectory
$D_{(t)}$	Orientation compartment index corresponding to position $\mathbf{p}_{(t)}$
$\rho^{[D]}(\mathbf{x})$	The ODF value sampled at orientation $\mathbf{v}_i^{[D]}$ at voxel location $\mathbf{x}$
$\mathbf{v}_{(t)}$	Local tract orientation corresponding to position $\mathbf{p}_{(t)}$
$\boldsymbol{\mu}$	Mean orientation of a Watson distribution
κ	Concentration parameter of a Watson distribution
$\boldsymbol{\mu}_{(t)}^{\left[D_{(t)}\right]}$	The D-th mean orientation corresponding to location $\mathbf{p}_{(t)}$
$\kappa_{(t)}^{\left[D_{(t)}\right]}$	The D-th concentration parameter corresponding to location $\mathbf{p}_{(t)}$
$\lambda_1, \lambda_2, \lambda_3$	Eigenvalues of a dyadic tensor; $\lambda_1 \geq \lambda_2 \geq \lambda_3$
N	Number of subjects

TABLE II

ROIs for Quantification of Fiber Crossings

Abbreviation	Description
CR-R	Corona Radiata (Right)
CR-L	Corona Radiata (Left)
OR-R	Optic Radiation (Right)
OR-L	Optic Radiation (Left)
CB-R	Cingulum Bundle (Right)
CB-L	Cingulum Bundle (Left)
SLF-R	Superior Longitudinal Fasciculus (Right)
SLF-L	Superior Longitudinal Fasciculus (Left)